CONSTRAINTS ON CHARON'S ORBITAL ELEMENTS FROM THE DOUBLE STELLAR OCCULTATION OF 2008 JUNE 22

B. Sicardy[1,2,3], G. Bolt[4], J. Broughton[5], T. Dobosz[6], D. Gault[7], S. Kerr[8], F. Bénard[9], E. Frappa[10], J. Lecacheux[1],
A. Peyrot[9], J.-P. Teng-Chuen-Yu[9], W. Beisker[11], Y. Boissel[1], D. Buckley[12], F. Colas[13], C. de Witt[14],
A. Doressoundiram[1], F. Roques[1], T. Widemann[1], C. Gruhn[15], V. Batista[16], J. Biggs[17], S. Dieters[18], J. Greenhill[18],
R. Groom[19], D. Herald[20], B. Lade[21], S. Mathers[22], M. Assafin[23], J. I. B. Camargo[23,24], R. Vieira-Martins[24],
A. H. Andrei[24], D. N. da Silva Neto[25], F. Braga-Ribas[1,24], and R. Behrend[26]

[1] Observatoire de Paris, LESIA, 5, Place Jules Janssen, 92195 Meudon Cedex, France
[2] Université Pierre et Marie Curie, 4 Place Jussieu, 75005 Paris, France
[3] Institut Universitaire de France, 103 boulevard Saint-Michel, 75005 Paris, France
[4] Craigie, 295 Camberwarra Drive, West Australia 6025, Australia
[5] Reedy Creek, 18 Branch Crescent, Queensland 4227, Australia
[6] Bankstown, 115 Oxford Avenue, Sydney 2200, New South Wales, Australia
[7] International Occultation Timing Association (IOTA) & Western Sydney Amateur Astronomy Group (WSAAG), Sydney, New South Wales, Australia
[8] Astronomical Association of Queensland & RASNZ Occultation Section, Glenlee, Queensland, Australia
[9] Association Astronomique de La Réunion (AAR), La Réunion Island, France
[10] Euraster, 1B Cours J. Bouchard, 42000 St-Etienne, France
[11] IOTA/ES, Bartold-Knaust-Strasse 8, D-30459 Hannover, Germany
[12] SAAO, P.O. Box 9, Observatory 7935, Republic of South Africa
[13] Observatoire de Paris, IMCCE, 61 Avenue de l'Observatoire, 75014 Paris, France
[14] Springbok, Northern Cape, Republic of South Africa
[15] Internationale Amateur Sternwarte (IAS), Hakos, Namibia
[16] Institut d'Astrophysique de Paris, 98bis Bld Arago, 75014 Paris, France
[17] Perth Observatory, 337 Walnut Rd., Bickley 6076, Western Australia, Australia
[18] School of Mathematics and Physics, University of Tasmania, PB 37 GP0 Hobart, Tasmania 7001, Australia
[19] Astronomical Society of Western Australia, P.O. Box 421, Subiaco, Perth, Western Australia 6904, Australia
[20] Canberra Astronomical Society and IOTA, Canberra, Australia
[21] Stockport Observatory, South Australia, Australia
[22] Southern Cross Observatory, Tasmania 42 South, University of Tasmania, PB 37 GP0 Hobart, Tasmania 7001, Australia
[23] Observatório do Valongo/UFRJ, Ladeira Pedro Antonio 43, CEP 20.080-090 Rio de Janeiro-RJ, Brazil
[24] Observatório Nacional/MCT, R. General José Cristino 77, CEP 20921-400 Rio de Janeiro-RJ, Brazil
[25] Centro Universitário Estadual da Zona Oeste, Av. Manual Caldeira de Alvarenga 1203, CEP 23.070-200 Rio de Janeiro-RJ, Brazil
[26] Observatoire de Genève, CH-1290 Sauverny, Switzerland

ABSTRACT

Pluto and its main satellite, Charon, occulted the same star on 2008 June 22. This event was observed from Australia and La Réunion Island, providing the east and north Charon Plutocentric offset in the sky plane (J2000): $X = + 12{,}070.5 \pm 4$ km ($+ 546.2 \pm 0.2$ mas), $Y = + 4{,}576.3 \pm 24$ km ($+ 207.1 \pm 1.1$ mas) at 19:20:33.82 UT on Earth, corresponding to JD 2454640.129964 at Pluto. This yields Charon's true longitude $L = 153.483 \pm 0°071$ in the satellite orbital plane (counted from the ascending node on J2000 mean equator) and orbital radius $r = 19{,}564 \pm 14$ km at that time. We compare this position to that predicted by (1) the orbital solution of Tholen & Buie (the "TB97" solution), (2) the PLU017 Charon ephemeris, and (3) the solution of Tholen et al. (the "T08" solution). We conclude that (1) our result rules out solution TB97, (2) our position agrees with PLU017, with differences of $\Delta L = + 0.073 \pm 0°071$ in longitude, and $\Delta r = + 0.6 \pm 14$ km in radius, and (3) while the difference with the T08 ephemeris amounts to only $\Delta L = 0.033 \pm 0°071$ in longitude, it exhibits a significant radial discrepancy of $\Delta r = 61.3 \pm 14$ km. We discuss this difference in terms of a possible image scale relative error of 3.35×10^{-3} in the 2002–2003 *Hubble Space Telescope* images upon which the T08 solution is mostly based. Rescaling the T08 Charon semi-major axis, $a = 19{,}570.45$ km, to the TB97 value, $a = 19636$ km, all other orbital elements remaining the same ("T08/TB97" solution), we reconcile our position with the re-scaled solution by better than 12 km (or 0.55 mas) for Charon's position in its orbital plane, thus making T08/TB97 our preferred solution.

Key words: astrometry – Kuiper belt objects: individual (Pluto, Charon) – occultations – planets and satellites: fundamental parameters

Online-only material: color figures

1. INTRODUCTION

On 2008 June 22, Pluto occulted the UCAC2 star 25370733 ($V = 12.4$, $R = 12.5$). This event was recorded from five stations in Australia and about 13 minutes later, the same star was occulted by Pluto's main satellite Charon, as seen from one station on La Réunion Island.

As such, this was a unique opportunity to directly measure in kilometers the distance of Pluto and its main satellite in the plane of the sky, at a given moment. This yields a new, independent constraint on Charon's orbit, since previous methods used mutual events observed in the late 1980s, speckle interferometry, and, more recently, images taken by the *Hubble Space Telescope* (*HST*) or ground-based telescopes—see a review in Tholen &

<div align="center">

Table 1
Pluto and Charon Adopted Physical Quantities

</div>

Quantity	Value
Pluto's mass[a]	$GM = 8.707 \times 10^{11}$ m^3 s^{-2}
Pluto's north pole[b] (J2000)	$\alpha_p = 313°0539$, $\delta_p = 6°1680$
Sub-observer and sub-solar latitudes	$B = -41°2$, $B' = -41°2$
Pluto's north pole position angle	$P = 65°3$
Charon's orbit pole[b] (J2000)	$\alpha_p = 133°0539$, $\delta_p = -6°1680$
Charon's radius	$R_C = 605 \pm 3$ km
Coordinates of occulted star, 2008 June 22 (J2000, UCAC2 system)	$\alpha_s = 269°6375575$, $\delta_s = -17°0439858$
Distance to observer, 2008 June 22, 19:10 UT	4.55833×10^9 km[c]
Nitrogen molecular mass[d]	$\mu = 4.652 \times 10^{-26}$ kg
Nitrogen molecular refractivity[e]	$K_{N_2} = 1.091 \times 10^{-23} +$ $(6.282 \times 10^{-26}/\lambda_{\mu m}^2)$ cm^3 molecule^{-1}

Notes.
[a] R. A. Jacobson (2005, private communication). Tholen et al. (2008) give a consistent value $8.703 \pm 0.037 \times 10^{11}$ m^3 s^{-2}, with a negligible difference as GM is solely used to calculate the acceleration $g = GM/r^2$.
[b] We used the IAU convention for Pluto's north and south poles, whereas in their Table 4, Tholen et al. (2008) used the opposite (angular momentum) convention.
[c] Corresponding to a scale of 22,099 km arcsec^{-1} at Pluto and a light travel time of 4.22360 hr.
[d] Assumed to be the only constituent in the ray tracing code, see the text.
[e] Washburn (1930).

Buie (1997), and more details in Buie et al. (2006) and Tholen et al. (2008).

Although internal accuracies at a few milliarcseconds (mas) can be reached with imaging techniques,[27] they all potentially suffer from two kinds of systematic errors: (1) the displacement of the center of mass and the center of light of objects—especially Pluto—may reach several tens of kilometers, possibly mimicking an orbital eccentricity for Charon, and (2) small errors in the scale and orientation of images may induce a systematic expansion (or shrinking) of Charon's orbital radius, plus a small rotation in the plane of the sky. For instance, a relative error of 10^{-3} in pixel scale causes a change of about 20 km in Charon's semi-major axis. Similarly, mutual events have their own scaling problems, in the absence of an accurate (km-level) determination of Pluto's radius, due to unmodeled albedo features on both Pluto and Charon.

In contrast, a double stellar occultation by Pluto and Charon allows in principle a direct determination of the positions of their physical centers at kilometric accuracy, independent of albedo features or scaling factors. A limitation of this method, however, is that occultations involving both Pluto and Charon are rare events, so that a good coverage of Charon's orbital longitudes is generally not possible. Also, potential biases stem from the fact that this method relies on a good synchronization in absolute time (down to a fraction of second) of all the clocks involved in the experiment. This may be problematic when various methods and equipment are used on various continents. As Pluto and Charon's shadow velocities on Earth were close to 24 km s^{-1} on 2008 June 22, a 1 s error on one clock directly results in a 24 km shift of the corresponding occultation chord in the plane of the sky. Also, as Pluto occultation light curves are not sharp due to the presence of a tenuous atmosphere, retrieving Pluto's center from an occultation event will depend on the atmospheric model used to fit the light curves, potentially introducing further systematic biases.

In this paper, we derive an accurate (better than $\sim$25 km) Plutocentric position for Charon at a given time on 2008 June 22. We discuss potential sources of errors in our approach. We then compare this position to that predicted by currently available sets of Charon's orbital elements, specifically (1) the one used to generate the PLU017 Charon ephemeris available online on the "Horizons" Jet Propulsion Laboratory (JPL) page (see Giorgini et al. 1996 and http://ssd.jpl.nasa.gov/horizons.cgi), (2) the orbital elements published by Tholen & Buie (1997; "TB97" solution), and (3) the solution of Tholen et al. (2008; "T08" solution), mainly based on *HST* images taken in 2002–2003.

2. PREDICTIONS

The occulted star was initially listed as P570 and C570 in McDonald & Elliot (2000) and was subsequently observed by our team in order to improve the predictions of the shadow tracks on Earth. Those observations were conducted independently at the Swiss 1.2 m telescope at La Silla, Chile in 2007 June and August; at the 2.2 m telescope of the European Southern Observatory (ESO) at la Silla, Chile in 2007 September and October; and at the 0.6 m telescope of the Laboratório Nacional de Astrofísica (LNA) at Pico dos Dias, Brazil in 2008 May. The methods and results concerning the 2.2 m ESO and 0.6 m occultation predictions are detailed in Assafin et al. (2010). Typical scatter between the various positions obtained during those campaigns is 30 mas. An analysis of those data eventually provided the following J2000 position for the star, in the UCAC2 system: $\alpha_s = 269°6375575$ and $\delta_s = -17°0439858$, as reported in Table 1.

This position slightly differs from the one published in Assafin et al. (2010), at the 10 mas level or so, due to small improvements made in that paper. This difference is not relevant in the present paper, as we will not discuss the absolute positions of Pluto and Charon in the sky. Instead, we are interested in the *differential* position of Pluto and Charon, so that any error on

---

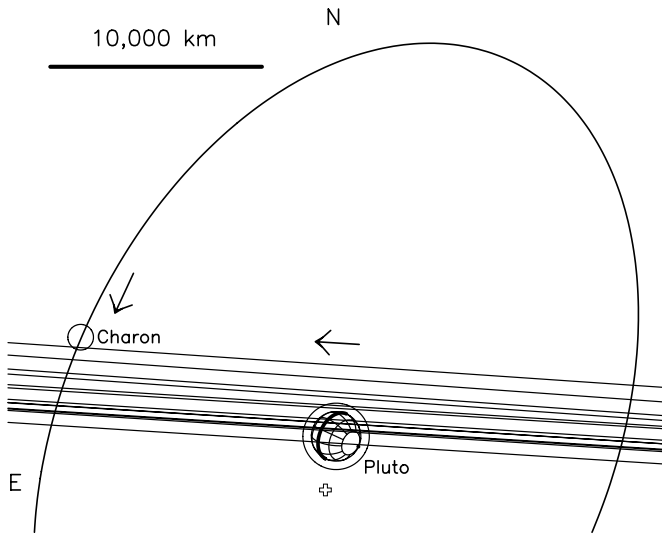[27] 1 mas corresponds to about 22 km at Pluto.

Figure 1. Geometry of the double 2008 June 22 stellar occultation. Labels N and E show the J2000 celestial north and east directions, respectively. Pluto's position is derived from a fit to the Australian light curves, using an atmospheric model (see Figures 2 and 6). The cross under Pluto shows the expected position of the planet center, according to the measured star position (Table 1) and the JPL DE413/PLU17 ephemeris. The mismatch with the observed position measures the offset between that ephemeris and the actual planet position, see details in Assafin et al. (2010). Charon's position expected from the PLU017 ephemeris is shown at left, at stellar closest approach time with the satellite at Les Makes (69633.82 s UT, see Table 4). The left arrow shows the direction of Charon's orbital motion. The central arrow shows the direction of stellar motions relative to Pluto, as seen from the various stations, and drawn here as oblique lines. See Figures 2 and 3 for details.

the star position will cancel out when deriving Charon's position with respect to Pluto.

The paths of Pluto and Charon's shadows on Earth, reconstructed after the occultation, are shown in Figure 8 of Assafin et al. (2010). In that figure, the locations of the various stations involved in that campaign are marked as gray star symbols.

3. OBSERVATIONS

Table 2 lists the various sites involved in this campaign and their coordinates, the equipment used, timing methods, and observers. Five stations in Australia were successful in recording the Pluto event (Bankstown, Blue Mountains, Reedy Creek, Glenlee, and Craigie, near Perth,[28] from south to north). One station at Les Makes observatory on La Réunion Island, in the Indian Ocean, observed the Charon event. Timing methods and their possible drawbacks are examined in more detailed in Section 6.2.

Figure 1 shows a general view of the star trajectories with respect to Pluto's system, as seen from the various stations listed in Table 2 (including negative observations). As we will see later, Charon was coincidently close to its expected pericenter at the moment of occultation (see Figure 10). Figures 2 and 3 show more detailed views centered on Pluto and Charon, respectively. In those figures, we have drawn in red the five Pluto occultation chords positively detected in Australia and the Charon occultation chord recorded at Les Makes.

Aperture photometry was performed in order to obtain the various occultation light curves, see Figures 6 and 7. Low frequency variations of signal outside the occultation were fitted

---

[28] There were two other stations, denoted "Perth" and "Perth bis" with negative results; see Table 2.
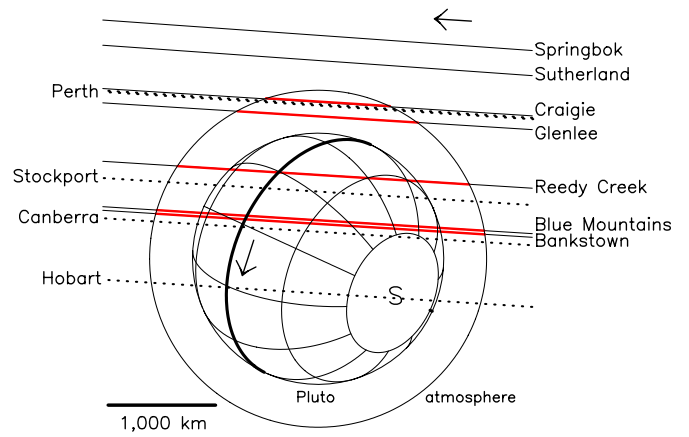

Figure 2. Enlargement of Figure 1, centered on Pluto. The solid stellar trajectories correspond to the stations were observations (positive or negative) could be made. The dotted trajectories are for stations which were clouded out, or with technical problems (no data). Pluto's radius, 1170 km, has been set arbitrarily to its minimum expected value (Lellouch et al. 2009). The circle around the planet has a radius of 1569 km, where the stellar flux is expected to drop by 1% of its unocculted value, according to the atmospheric model shown in Figure 4. The upper arrow indicates the star motion relative to the dwarf planet. The central arrow shows the direction of Pluto's rotation, and the letter "S" marks the position of the planet south pole (IAU convention). The red segments indicate the five positive occultation detections and correspond to the time intervals where the stellar flux dropped by more than 1%, see also Figure 6.

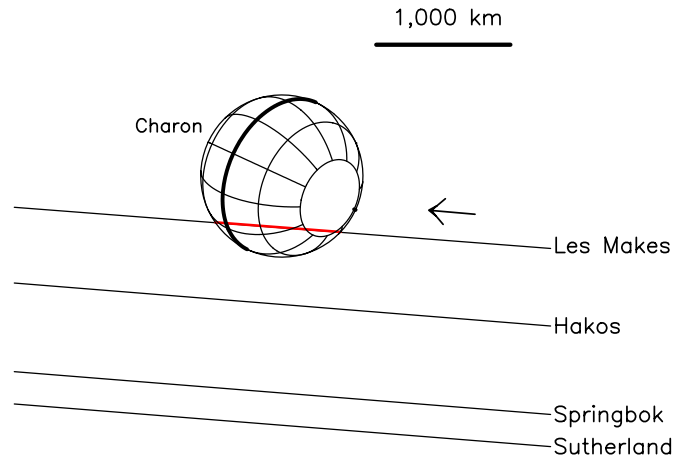(A color version of this figure is available in the online journal.)

Figure 3. Enlargement of Figure 1, centered on Charon. The red segment corresponds to the time interval of the Charon occultation observed at Les Makes (La Réunion Island), see also Figure 7.

(A color version of this figure is available in the online journal.)

with a polynomial of degree 3, which served to normalize the stellar flux $\Phi_{\rm star}$ to unity outside the event.

Images of the same field of view were taken at Bankstown several days after the Pluto event (on 2008 August 14) for photometric calibration purposes, using the same equipment and at same airmass as for the occultation at that site. Three reference stars were used to estimate the flux of the target and then assess the contribution of Pluto's flux $\Phi_{\rm Pluto}$ to the occultation light curve. We find a ratio $\Phi_0 = \Phi_{\rm Pluto}/(\Phi_{\rm star} + \Phi_{\rm Pluto}) = 0.178$ (also called the "zero stellar flux level"), with a formal 1σ error of ± 0.004.

This value appears too high, however, when compared to the flux observed at the bottom of the occultation in Bankstown, which is estimated between 0.16 and 0.17. This would imply that the residual stellar flux during the occultation becomes negative,

Table 2
Circumstances of Observations

Site Name	Lat. (d:m:s) Lon. (d:m:s) Alt. (m)	Telescope Aperture Instrument/Receptor Remarks	Timing Method Integration (s) Cycle Time (s) Start/End Recording (UTC)[a]	Observers
Australia				
Hobart	42:50:49.8 S 147:25:54.5 E 287	40 cm . . . Clouded out	. . . .	V. Batista J. Greenhill
Canberra	35:23:49.3 S 149:03:49.0 E 140	35 cm . . . Clouded out	. . . .	D. Herald
Bankstown	33:55:56 S 151:01:45 E 24.9	27.5 cm Video, broad band Pluto event detected	GPS time inserter[b] 1.28 1.28 19:04:03/19:10:36	T. Dobosz
Blue Mountains	33:39:51.9 S 150:38:27.9 E 286	25 cm Video, broad band Pluto event detected	GPS time inserter[b] 1.28 1.28 19:06:13/19:08:46	D. Gault
Stockport	34:19:55.31 S 138:43:45.38 E 142	50 cm . . . Clouded out	. . . .	B. Lade
Reedy Creek	28:06:29.9 S 153:23:52.0 E 65	25 cm CCD, broad band Pluto event detected	Shutter audio analysis[c] 6.30 8.82 19:05:58/19:08:29	J. Broughton
Glenlee	23:16:09.6 S 150:30:00.8 E 50	30 cm Video, broad band Pluto event detected	GPS time inserter[b] 0.12 0.12 19:05:00/19:09:01	S. Kerr
Craigie	31:47:21.5 S 115:45:31.3 E 45	25 cm CCD, broad band Pluto event detected	PC time[d] 2.0 6.0 19:00:06/19:30:58	G. Bolt
Perth	32:00:28.6 S 116:08:06.0 E 428	40 cm Video, broad band Technical failure	GPS time inserter	J. Biggs
Perth bis	31:52:53.0 S 116:10:12.3 E 260	30 cm CCD Too long exposures	Internet time update 10 24.4 . . .	R. Groom
Republic of South Africa				
Sutherland (SAAO)	32:22:46.0 S 20:48:38.5 E 1760	100 cm Video, broad band No event detected	GPS time inserter[b] 0.167 0.167 . . .	F. Colas
Sutherland (SAAO)	32:22:46.0 S 20:48:38.5 E 1760	193 cm Video, broad band No event detected	GPS time inserter[b] 0.083 0.083 . . .	F. Colas
Springbok	29:39:40.2 S 17:52:58.8 E 900	30 cm CCD, broad band No event detected	PC time[e] 2 2 . . .	T. Widemann C. de Witt
Namibia				
Hakos	23:14:42.0 S 16:21:12.0 E 1834	50 cm CCD, broad band, visual monitoring of CCD display No event detected (see the text)	GPS time 0.1 0.1 . . .	C. Gruhn
France				
Les Makes	21:11:57.4 S 55:24:34.5 E 972	35 Video, broad band Charon event detected	GPS time inserter[b] 0.32 0.32 19:20:02/19:21:02	J. P. Teng F. Benard

Notes.

[a] Start and end of recording is given for the experiments that provided positive events. Data acquired in the Republic of South Africa were taken through passing clouds and only a visual inspection of the images were made near the expected time of the Charon occultation to check for a possible event.

[b] Kiwi OSD system; see the text.

[c] Set against WWVH clock; see the text.

[d] Set against internet NPT server; see the text.

[e] PC time set by GPS before observation and drift checked after observation.

which is impossible. This means that our relative photometric calibration has some inconsistencies at the level of 1%–2%. This may be due to changing extinction conditions between the two observations, which changed the apparent colors of the stars, and thus their relative brightness, in our broadband experiments. Other effects (small inconsistencies in flat fielding procedures, uncontrolled effects of the particular value of the apertures used, etc.) are possible. In the absence of clear answers about those points, and also because the lack of calibration at the other stations, we decided not to use the value $\Phi_{\mathrm{Pluto}}/(\Phi_{\mathrm{star}} + \Phi_{\mathrm{Pluto}})$ quoted above when fitting the Pluto light curves. Instead, we consider this quantity as a free parameter in the fit (see the next section).

4. ASTROMETRIC RECONSTRUCTION OF THE EVENT

If the star position and Pluto's ephemeris were exact, we would know at each moment the position of an observing site with respect to the planet shadow on Earth or equivalently the position of the star relative to the planet projected in the plane of the sky, as seen from that site.

Let us denote (f, g) the position—measured in kilometers —of the star image projected in the sky plane, relative to Pluto's center, where f (resp. g) is counted positively toward the local celestial J2000 east (resp. north) direction. In practice, however, there are errors on both the star position and on Pluto's ephemeris. Their combined values are of the order of 0.1 arcsec, corresponding to several hundreds of kilometers when projected at the planet.

Consequently, an offset $(\Delta f_P, \Delta g_P)$—called here "Pluto's offset" for the sake of brevity—has to be applied to Pluto's ephemeris in the sky plane in order to fit the observations. Again, Δf_P (resp. Δg_P) are counted positively eastward (resp. northward). With that convention, the actual star position relative to Pluto's center in the plane of the sky is $(f - \Delta f_P, g - \Delta g_P)$.

The same is true for Charon, for which we must know not only the general motion of Pluto's system in the plane of the sky (i.e., Pluto's ephemeris) but also the satellite motion around the dwarf planet (i.e., Charon's Plutocentric ephemeris). Again, an offset $(\Delta f_C, \Delta g_C)$—called here "Charon's offset"—has to be applied to Charon's position in the plane of the sky in order to match the observations.

If Charon's Plutocentric ephemeris were exact, then Pluto's and Charon's offsets would be equal,[29] i.e., $(\Delta f_P, \Delta g_P) = (\Delta f_C, \Delta g_C)$. Conversely, a non-zero difference $(\Delta f_C - \Delta f_P, \Delta g_C - \Delta g_P)$ will reveal a discrepancy between Charon's observed and calculated planetocentric positions X and Y projected in the plane of the sky, where X (resp. Y) is Charon's offset with respect to Pluto in the local celestial J2000 east (resp. north) direction.

In the following, and unless explicitly stated, we will use the *JPL* DE413 barycentric ephemeris for Pluto's system, and the *JPL* PLU017 Charon's Plutocentric ephemeris as our reference against which the respective Pluto and Charon offsets will be derived.

[29] This reasoning assumes that the star position did not change between the 13 minutes or so separating the Pluto and Charon events. As the star proper motion is less than 10 mas year^{-1} as given by the UCAC2 catalog (Ochsenbein et al. 2000), the star position changed by less than 3×10^{-4} mas between the two occultations, corresponding to less than 5 m when projected at Pluto. This is negligible at the level of accuracy considered here.
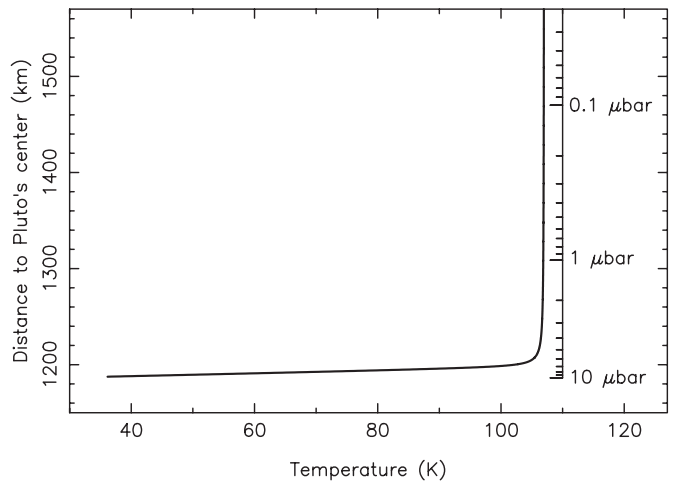

Figure 4. Atmospheric model used for the fits in Figure 6. The temperature T is shown as a function of distance r to Pluto's center. The pressure scale p is shown at right. The $T(r)$ profile is composed of a hyperbolic branch, according to Equation (A2). The profile starts at $r_0 = 1187.5$ km, with $T_0 = 36.1$ K and $p_0 = 9.82$ μbar. At $r = 1215$ km, pressure has dropped to $p_{1215} = 5.06$ μbar. The deep inversion layer starts with a gradient of +7 K km^{-1} and then connects itself with an isothermal branch with $T = 107$ K above $r \approx 1210$ km.

4.1. Pluto's Offset

4.1.1. Light-curve Fitting

Because of Pluto's atmosphere, there are no sharp disappearances and reappearances of the star during the event, see Figure 6. Consequently, we have to simultaneously fit synthetic occultation light curves to the five corresponding data sets in order to retrieve Pluto's center position.

Those synthetic light curves are generated using a ray tracing code, based on a given density profile $n(r)$ as a function of radius r (the distance to Pluto's center), assuming a pure molecular nitrogen N_2 atmosphere. This provides us with the refractivity profile $\nu(r) = n(r)/K_{N_2}$, where K_{N_2} is the nitrogen molecular refractivity, see Table 1 for numerical values. Since we have several chords, we might also include a distortion in the atmosphere—for instance we could use an elliptic shape with given ellipticity and position angle. We have actually tried to individually fit each light curve using the atmospheric model of Figure 4 described below in order to detect variations of a given isobar radius with latitude. However, it turns out that the radius of a given reference level (e.g., the so-called half-light level) is strongly correlated with the assumed contribution of Pluto to the total star + Pluto flux observed during the occultation. This calibration is not available, or not accurate enough, to be added as a further constraint in our model. Consequently, we assume that the atmosphere is spherically symmetric in our fitting procedure. This hypothesis is discussed later in this paper (see Section 6.1).

The ray tracing code uses the $n(r)$ profile, which is based in turn on a given temperature profile $T(r)$ and a boundary condition, more precisely the pressure p at a given radius r, using hydrostatic equilibrium and ideal gas law. Details on how the profiles are generated are given in the Appendix (see in particular Equations (A1) and (A2)). Our nominal temperature profile $T(r)$ with associated pressure levels is shown in Figure 4. The $T(r)$ profile described by Equation (A2) is characterized by a lower inversion layer with a strong temperature gradient $(dT/dr)_i = 7$ K km^{-1}. It starts at a minimum radius (deepest point) of $r_0 = 1187.5$ km where the pressure is maximum at

$p_0 = 9.82$ μbar and then connects itself to an upper isothermal branch at $T_\infty = 107$ K, with a pressure value of $p = 5.06$ μbar at the particular radius of $r = 1215$ km. The transition between the inversion layer and the isothermal branch (the "knee" in the temperature profile) occurs 9.9 km above r_0, specifically at a radius $r_k = r_0 + 9.9 = 1197.4$ km.

For the moment, all the parameters r_0, p_0, r_k, $(dT/dr)_i$, and T_∞ are fixed. The propagation of the error bars on those quantities into the retrieved Pluto's center position is examined later. The main goal of the nominal profile is to capture the basic structure of Pluto's atmosphere, namely, a deepest region close to the surface at 35–40 K, followed by a rapid temperature increase caused by methane absorption in the near IR, and finally, a methane-regulated isothermal upper branch at $T \sim 100$ K (Yelle & Lunine 1989). Note that we ignore the possible existence of a troposphere below $r_0 = 1187.5$ km. This would introduce some complications in the modeling but would have a minimal impact on the results of our present fitting procedure. This point is discussed further in Section 4.1.2.

The four free parameters of the fit are Pluto's offsets in right ascension (Δf_P) and declination (Δg_P), the pressure boundary condition p_0, assuming a fixed temperature profile, and the zero stellar flux Φ_0 defined in the previous section. Pluto's offset was split in two parts. One part is along Pluto's motion, Δl (counted positively eastward), and is entirely determined by the timing of the event at the various stations. The other part is perpendicular to Pluto's motion, $\Delta\rho$ (counted positively northward), and controls the distance of closest approach of each station to Pluto's shadow center. An appropriate transformation taking into account the orientation of Pluto's motion in the sky plane then relates $(\Delta l, \Delta\rho)$ to $(\Delta f_P, \Delta g_P)$.

A classical χ^2 minimization was performed to find the best fit to the data, with $\chi^2 = \sum_i (\Phi_{i,\mathrm{obs}} - \Phi_{i,\mathrm{the}})^2/\sigma_i^2$, where $\Phi_{i,\mathrm{obs}}$ is the observed flux at the ith point, $\Phi_{i,\mathrm{the}}$ is the corresponding theoretical flux calculated through the ray tracing code, and σ_i is the uncertainty on data estimated from the rms scatter outside the occultation, when this was possible. Too few data points are available from Blue Mountains and Reedy Creek, so σ_i was directly estimated from the rms dispersion for the best fit.

The minimization process separated the determination of Δl and Φ_0 from the determination of $\Delta\rho$ and p_0. The parameter Δl is largely independent of the particular Pluto's atmospheric model used (provided it remains spherically symmetric) and was determined once for all by varying Δl and taking the value which minimized χ^2 and yielded $\Delta l = -345 \pm 4$ km. The parameter Φ_0 was determined through a linear fit of the model to the data using classical least square formulae.

The remaining parameters $\Delta\rho$ and p_0 were obtained by generating synthetic light curves on a grid with 21 values for $\Delta\rho$ with steps of 5 km, and 31 values for p_0 with steps of 0.2 μbar, totaling $21 \times 31 = 651$ light curve generations for the five stations (i.e., 3255 calls of the ray tracing code), and picking the values of p_0 and $\Delta\rho$ which minimizes χ^2. The best-fitting solution was $p_0 = 9.82 \pm 0.43$ μbar at $r_0 = 1187.5$ km and $\Delta\rho = 2570 \pm 12$ km (1σ level). We also give here the pressure $p_{1215} = 5.06 \pm 0.22$ μbar at $r = 1215$ km for that same profile. The motivation for using p_{1215} is to permit an easier comparison with results from other teams, as $r_0 = 1187.5$ km is deeper than any levels probed so far by ground-based stellar occultations. Figure 5 shows the aspect of the iso-χ^2 curves in the $(p_{1215}, \Delta\rho)$ plane.

In total 3864 data points were used for the five stations (236 for Bankstown, 307 for Blue Mountains, 18 for Reedy Creek,
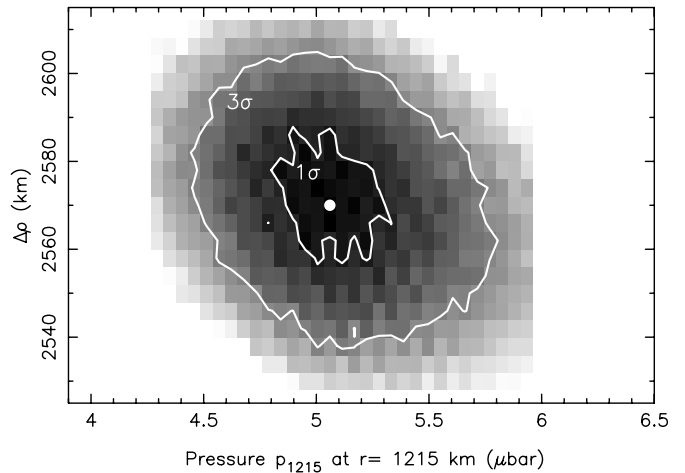

Figure 5. χ^2-map for the simultaneous fit to the five Australian Pluto light curves. Darker zones correspond to lower value of χ^2. The white dot shows the best fit, at $p_{1215} = 5.06 \pm 0.22$ μbar, $\Delta\rho = 2570 \pm 12$ km (1σ level), and corresponds to a minimum value $\chi^2_{\min}$ per degree of freedom of 0.97, see Table 3, Figure 6, and the text for details. The 1σ level is delineated by the inner closed curve ($\chi^2_{\min} + 1$ level). The outer closed curve corresponds to the 3σ level ($\chi^2_{\min} + 9$ level).

3251 for Glenlee, and 52 for Craigie). The best fit provides a $\chi^2_{\min}$ per degree of freedom of 0.97, and is shown in Figure 6. This indicates a correct fitting of the model to the data, considering the uncertainties of the measurements, the latter being dominated by photometric noise. Quoted errors are internal errors at 1σ level, and are derived using the usual $\Delta\chi^2 = \chi^2 - \chi^2_{\min} = 1$ criterion around the best fit. Similarly, the 3 σ levels shown in some of the figures are derived from the usual $\Delta\chi^2 = \chi^2 - \chi^2_{\min} = 9$ criterion, see Figure 5.

From the values of Δl and $\Delta\rho$ determined above, we derive the following offset for Pluto (body center), with respect to the DE413/PLU017 ephemeris: $\Delta f_P = -505.9 \pm 4$ km and $\Delta g_P = +2543.2 \pm 12$ km. The quoted error bars are internal to the fit. Larger errors stemming from our assumptions on Pluto's atmosphere structure are discussed below. Relevant values corresponding to this best fit are summarized in Table 3, where again all quoted error bars are internal to the fit, i.e., smaller than the more realistic error bars discussed now.

4.1.2. Sensitivity to the Atmospheric Parameters

The nominal temperature profile used so far (see Figure 4 and Equation (A2)) starts at $r_0 = 1187.5$ km, with a pressure $p_0 = 9.82$ μbar and a temperature gradient $(dT/dr)_i = 7$ K km^{-1} in the inversion layer, a knee at $r_k = 1197.4$ km, followed by an upper isothermal part with $T_\infty = 107$ K.

We first examine the sensitivity of the $(\Delta f_P, \Delta g_P)$ retrieval to $(dT/dr)_i$, keeping the profiles $T(r)$ and $p(r)$ unchanged above r_k. Varying $(dT/dr)_i$ modifies the synthetic light curves below a fractional stellar flux of ~ 0.2. Its main effect is to change the residual stellar flux at the flat, bottom part of the light curve. More precisely, the higher that gradient, the lower the residual flux. Our photometric calibrations of the 2008 June 22 data are not accurate enough to derive this residual flux. However, an occultation observed two days later (2008 June 24) in K band at the Canada–France–Hawaii Telescope shows that the residual stellar flux lies between 1.5% and 2.3% of the unocculted stellar flux (B. Sicardy et al. 2011, in preparation). From these figures, we deduce that $(dT/dr)_i$ lies in the range of 7 ± 3 K km^{-1}. We have fitted the data with p_{1215} and $\Delta\rho$ as free parameters, varying

Table 3
Astrometric Reconstruction from Pluto Atmospheric Fit (Australia)

Station	Time of Closest Approach to Shadow Center[a] (UT, s)	Distance of Closest Approach to Shadow Center[b] (km)	Ingress Latitude[c] (deg)	Egress Latitude[c] (deg)
Bankstown	68848.6 ± 0.25	$+313.9 \pm 12$	-39	$+48$
Blue Mountains	68848.1 ± 0.25	$+347.9 \pm 12$	-38	$+48$
Reedy Creek	68832.1 ± 0.50	$+769.0 \pm 12$	-28	$+48$
Glenlee	68823.1 ± 0.60	$+1313.5 \pm 12$	-09	$+37$
Craigie	68904.7 ± 3.30	$+1451.2 \pm 12$	00	$+31$
Retrieved Pluto occultation geometry				
Pluto's offset[d]	$\Delta f_P = -505.9 \pm 4$ km			
	$\Delta g_P = +2543.2 \pm 12$ km			
Pressure boundary condition[e]	$p_{1215} = 5.06 \pm 0.22 \mu$bar at $r = 1215$ km			

Notes. All the error bars quoted in this table are 1σ level and are internal to the fit. Larger error bars due to various possible biases are discussed in the text.
[a] 2008 June 22.
[b] Positive values mean that observers went north of shadow center.
[c] Corresponding to the 99% level of unocculted stellar flux.
[d] With respect to the JPL DE413/PLU017 ephemeris, see the text.
[e] Using the temperature profile of Figure 4, see also Equation (A2).

$(dT/dr)_i$ in the range 4–10 K km^{-1}. We then observe changes of $\Delta\rho$ by ± 5 km at most, i.e., we see vertical displacements of the whole pattern of Figure 5 by ± 5 km. This means that the error bar on Pluto's center associated with the uncertainty on $(dT/dr)_i$ is also ± 5 km, essentially in the north–south direction.

Note that this gradient is expected from solar absorption in the near-IR and radiation at 7.7 μm in methane lines, combined with conduction from the cold ice surface. Assuming a 0.3% CH$_4$ mixing ratio and a surface (or tropopause) pressure of 3μbar, Strobel et al. (1996) derive an expected gradient of $(dT/dr)_i \approx 7$–8 K km^{-1} in the inversion layer. Although the recent derivation of the CH$_4$ mixing ratio by Lellouch et al. (2009) provides a slightly different value (0.5% $\pm$ 0.1%), the range of 6–10 K km^{-1} that we explore here is clearly consistent with current Pluto's atmospheric models. Note also that what we actually need is a template for the occultation light curve. We use this template to fit the data and then retrieve Pluto's center position. So, even if extinction is responsible for some of the features observed in the deepest parts of the occultation light curves (e.g., the shape of the knee or the value of the stellar residual flux), the template is not changed, and neither is our astrometric reconstruction.

The next parameter that we varied is T_∞, keeping the lower part of the profile unchanged, i.e., using the nominal pressure and temperature profiles between r_0 and r_k. The minimum value of χ_m^2 then obtained with a global fit to all five light curves corresponds to $T_\infty = 107 \pm 3.5$ K, the error bar stemming from the usual $\chi_m^2 + 1$ criterion. Our value for T_∞ is consistent with other results in 1988, 2002, and 2006, e.g., $T_\infty = 104 \pm 2$ K (Pasachoff et al. 2005), $T_\infty = 102 \pm 4$ K on average (Elliot et al. 2007), $T_\infty \approx 101$ K (Sicardy et al. 2003), and $T_\infty = 104 \pm 3$ K (Young et al. 2008). Elliot et al. (2007) and Young et al. (2008) also evoke the detection of a small negative temperature gradients of ~ -0.1–0.2 K km^{-1} in the (almost) isothermal upper part, possibly associated with CO cooling. However, those modest gradients can be absorbed in an equivalent isothermal profile, as a light curve generated with a small negative (resp. positive) gradient is undistinguishable

from a light curve generated with an isothermal profile with slightly higher (resp. smaller) temperature, see Equation (A1).

Taking T_∞ in an extreme interval of 100–115 K and performing best fits with those extreme values change $\Delta\rho$ by ± 5 km at most, comparable to the effect of $(dT/dr)_i$ assessed above.

We now examine the potential effect on $\Delta\rho$ of a deep troposphere below the deepest level considered so far, $r_0 = 1187.5$ km. The existence of such troposphere was first discussed by Stansberry et al. (1994), with possible depths as large as 40 km. More recently, Lellouch et al. (2009) have combined occultation observations made since 2002 and high-resolution spectroscopic observations of gaseous methane to put more stringent constraints on such troposphere. If it exists, it should have a maximum depth of 17 km below $r_0 = 1187.5$ km, and a maximum pressure at the surface of $p \sim 24$ μbar. Thicker tropospheres would imply a column density of cold methane near the surface that would be incompatible with the observed methane spectral lines. In addition, the boundary condition p_0 must be adjusted so that to avoid that conspicuous caustics spikes, caused far limb stellar images produced in the troposphere, appear in the flat, low residual stellar flux part of the occultation, where they are not observed. However, those spikes are allowed in the steeper immersion or emersion parts of the occultation, where they could be mistaken for noise or usual atmospheric spikes caused by small temperature fluctuations.

Combining those constraints, Lellouch et al. (2009) conclude that a narrow range of parameters are possible for the temperature profiles, with $(dT/dr)_i$ values in the range 5–7 K km^{-1}, and tropospheric temperature gradient bracketed by the N$_2$ wet adiabat, ~ -0.1 K km^{-1}, and the N$_2$ dry adiabat, ~ -0.6 K km^{-1}. Using those extreme values, we find that including a troposphere with a wet gradient in our fitting procedure would increase the retrieved value of $\Delta\rho$ by about 5 km, while a dry tropospheric gradient would increase it by about 13 km. Thus, we estimate that the existence of a troposphere could introduce typical biases of ~ 10 km in the retrieved value of $\Delta\rho$.

We are left with a last potential problem concerning the profiles, namely, the absolute radius scale used in our nominal profile in Equation (A2). In other words, the entire profiles $T(r)$
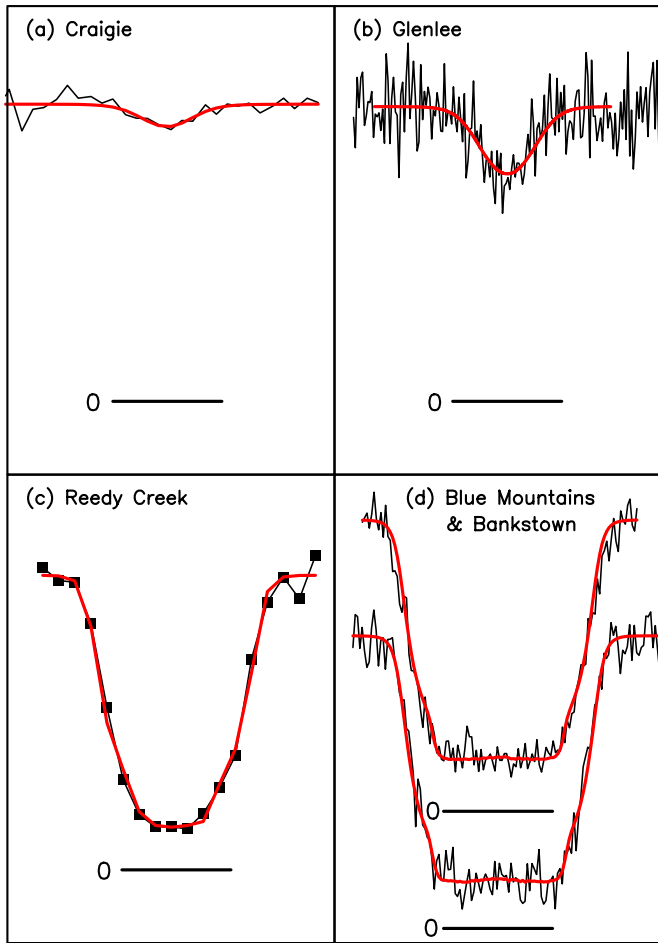
Figure 6. Simultaneous fits to the five Pluto occultation light curves obtained in Australia (corresponding to the positive chords drawn in Figure 2). Each panel has a duration of 3 minutes and all the light curves are plotted at the same vertical scale. The horizontal bars labeled "0" under each curve correspond to a 1 minute time interval, and also give the zero flux level for each light curve. Those bars are, respectively, centered at UT times of 68,905 s (panel (a)), 68,823 s (panel (b)), 68,832 s (panel (c)), and 68,848 s (panel (d)). The fact that the fluxes do not drop to zero at mid-occultation in panels c and d stems from Pluto's contribution to the total recorded flux, see the text for details.

(A color version of this figure is available in the online journal.)

and $p(r)$ may be shifted vertically by a mere change of r_k. Unfortunately, the chords that we have at hand are distributed on only one side of the dwarf planet, see Figure 2. This means that there is a strong correlation between the assumed value of r_k (i.e., the global "size" of the atmosphere) and $\Delta\rho$. Practically, increasing r_k by 1 km, i.e., expanding all the isobars radii by 1 km, decreases the derived value of $\Delta\rho$ by nearly 2 km. In the absence of a good chord coverage, we have to rely upon other independent measurements which provide a reference radius for the atmosphere. The so-called half-light radius in Pluto's shadow, $r'_{1/2}$, may for instance serve as a benchmark. It corresponds to the distance of the observer to the shadow center where the stellar flux reaches the half of its unocculted value. Current published values for $r'_{1/2}$ are $r'_{1/2} = 1213 \pm 6$ km for the 2002 August 21 occultation (Elliot et al. 2003), $r'_{1/2} = 1208 \pm 4$ km, and $r'_{1/2} = 1216 \pm 8.6$ km for the 2006 June 12 occultation (see Elliot et al. 2007 and Young et al. 2008, respectively) and $r'_{1/2} = 1207 \pm 4$ km for the 2007 March 18 event (Person et al. 2008).

We thus estimate that a range of 1215 ± 10 km encompasses the possible values for $r'_{1/2}$. Our nominal profile with $r_0 = 1187.5$ km and boundary condition $p_0 = 9.82$ μbar actually provides the median value of $r'_{1/2} = 1215$ km for the half-light radius in the shadow plane.[30] Varying r_0 (and thus also $r'_{1/2}$) by ± 10 km will consequently vary $\Delta\rho$ by ± 20 km. This is the largest source of error on $\Delta\rho$, as far as the sensitivity on Pluto's atmospheric parameters is concerned. When combined with the internal 1σ error bar of ± 12 km obtained with the simultaneous fit (Equation (1)) and a possible bias of $\sim$10 km caused by a putative troposphere as discussed before, we arrive at an estimated error bar of ± 25 km for $\Delta\rho$. Note that this error bar represents about 40% of the density scale height at half-light level, $H_n \approx 60$ km.

Note also that the relative star–Pluto motion is essentially in the east–west direction (Figure 2). Consequently, the value of the error bar on Δf_P essentially depends on Δl, i.e., on the timing of the event, and very little on the particular value of p_0. Conversely, Δg_P essentially depends on $\Delta\rho$, which in turn depends on the assumed radii of the various isobar levels, i.e., eventually, on the assumed profile $T(r)$ and boundary condition p_0. So, we finally arrive at the following values for Pluto's offsets in right ascension and declination:

$$\begin{cases} \Delta f_P = -505.9 \pm 4\,\text{km}; & \Delta\alpha\cos\delta = -22.89 \pm 0.18\,\text{mas} \\ \Delta g_P = +2543.2 \pm 25\,\text{km}; & \Delta\delta = +115.08 \pm 1.0\,\text{mas}, \end{cases}$$

$$\tag{1}$$

where the offsets have also been converted to mas. It is important to note that the real error bars on Pluto's offsets are actually dominated by the error bars on the star position, which are much larger (at the $\sim$ 15–25 mas level) than the mas level quoted here. As explained before, though, errors on the star position eventually cancel out since we are only concerned here by Charon's position relative to Pluto. The problem of Pluto's offset evolution with time is discussed elsewhere (Assafin et al. 2010) and will not be considered here.

4.2. Charon's Offset

We have determined the disappearance (ingress) and reappearance (egress) times of the star behind Charon at Les Makes station, using a model which includes Fresnel's diffraction by a sharp edge, convolution by the instrumental bandwidth and by the stellar profile projected at Charon, and a final convolution accounting for the finite integration time for each data point, see Widemann et al. (2009) for more details on the method. For practical purposes, considering the integration time (0.32 s) and shadow velocity (about 24 km s^{-1}), the final synthetic occultation light curve shown in Figure 7 is largely dominated by the finite integration time, and little affected by diffraction, finite stellar size, and limb-darkening effects.

The derived ingress and egress times, and other quantities of interest, are listed in Table 4. These timings define a single occultation chord in the sky plane with length 937.9 ± 4 km, see also Figure 3. Two solutions are in principle possible for Charon's position since we have only one chord. However, the solution not shown would imply that a $\sim$48 s occultation should have occurred at Hakos between 19:22 and 19:23 UT. A camera

---

[30] The corresponding half-light radius in Pluto's atmosphere is then $r_{1/2} = 1279$ km. It can be compared to the values ranging from 1276 km to 1291 km obtained by the authors quoted before.
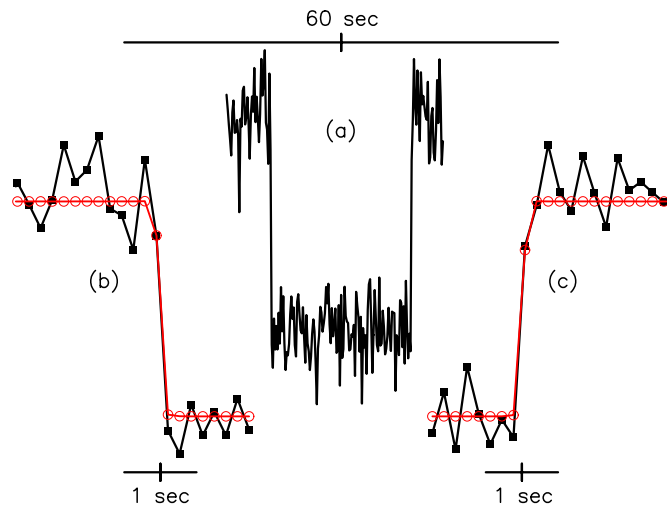
Figure 7. (a) The stellar occultation by Charon observed at Les Makes, corresponding to the red chord shown in Figure 3. The upper horizontal bar gives the 60 s time interval centered at stellar closest approach (tick mark), at 69633.82 s UT. (b) An expanded view of the ingress data points (black squares and line), with a timescale multiplied by a factor of 10 with respect to panel (a). The diffracting best-fit model is shown superimposed in red (red circles and line). The 1 s time interval is centered on the fitted ingress half-light time (tick mark), at 69614.40 s UT. (c) Same as panel (b), but for egress. The 1 s time interval is now centered on the fitted egress half-light time, at 69653.23 s UT.

(A color version of this figure is available in the online journal.)

Table 4
Astrometric Results Derived from Charon Occultation Fit (La Réunion)

Ingress (UT, s)[a]	Egress (UT, s)[a]
69614.40 ± 0.04	69653.24 ± 0.04
Reconstructed Charon occultation geometry	
Time of star closest approach (UT)[a]	69633.82 ± 0.03 s
Distance of star closest approach (km)[b]	−382.3 ± 4.9 km
Charon's offset[c]	$\Delta f_C = -495.4 \pm 0.8$ km
	$\Delta g_C = +2520.7 \pm 4.9$ km

Notes.
[a] 2008 June 22.
[b] Negative value means that the star went south of Charon's center in the sky plane, as seen from Les Makes.
[c] Based on a Charon radius of $R_C = 605 \pm 3$ km, see the text. Offset is with respect to DE413/PLU017 ephemeris; see the text.

was actually used at that site at a rate of 10 frames s^{-1} (Table 2). A software problem prohibited the recording of the data, but the observer could watch the screen showing the star at that rate. A 48 s disappearance of the star around 19:22–19:23 UT would have been clearly noticed by the observer, which was not the case. We thus eliminate this second solution hereafter.

As the ingress and egress times have uncertainties of 0.04 s, and Charon's velocity relative to the star is 24.15 km s^{-1} in the sky plane, the uncertainty on Charon's center position along its motion on the sky (essentially the east–west direction, see Figure 3) is $(0.04/\sqrt{2}) \times 24.15 \sim 0.7$ km. Since we have only one chord, we cannot specify the position of Charon's center perpendicular to celestial motion, unless we know its shape. We assume here that Charon is spherical and that its radius is that given by the 2005 July 11 occultation, observed in total from six stations (Gulbis et al. 2006; Sicardy et al. 2006a; Person et al. 2006). Charon's radius ranges from 604 ± 1.4 to 606 ± 1.5 km depending on authors. However, local topographic features at the level of 2–3 km may affect the local limb radius, see, e.g.,

the multi-chord occultation by Uranus' main satellite Titania of 2001 September 8 (Widemann et al. 2009), for which a radius of 788.4 km—comparable to Charon's—was derived.

Consequently, we consider a local limb radius of 605 ± 3 km (1σ level), with an error bar representative of Charon's topographic vertical variations. We use this range to evaluate the uncertainty on Charon's position perpendicular to its sky-plane motion when fitting the satellite limb to the chord, as shown in Figure 3. This uncertainty amounts to ± 4.8 km, and largely dominates the uncertainty associated with the timing errors of ± 0.04 s quoted earlier. Combining those various uncertainties (1σ level) provides Charon's offset with respect to the DE413/PLU017 ephemeris:

$$\begin{cases} \Delta f_C = -495.4 \pm 0.8 \, \text{km}; & \Delta\alpha\cos\delta = -22.42 \pm 0.04 \, \text{mas} \\ \Delta g_C = +2520.7 \pm 4.9 \, \text{km}; & \Delta\delta = +114.06 \pm 0.22 \, \text{mas}, \end{cases}$$
(2)

see also Table 4.

5. CHARON'S PLUTOCENTRIC POSITION

Equations (1) and (2) provide the difference between Charon's Plutocentric position, in the plane of the sky at the moment of occultation and the position expected from the PLU017 ephemeris: $\Delta f_C - \Delta f_P = +10.5 \pm 4$ km and $\Delta g_C - \Delta g_P = -22.5 \pm 24$ km. Note that error bars are dominated by the errors on Pluto's position, i.e., that the errors on Charon's position are negligible in our result. Using Charon's Plutocentric offset predicted by PLU017 (see Table 5) and adding the differences found above, we derive the following Charon's Plutocentric offset (X, Y) at occultation mid-time $(X, Y) = (+12, 070.5 \pm 4 \, \text{km}, +4, 576.3 \pm 24 \, \text{km})$.

Charon's position (X, Y) can be projected into Charon's orbital plane, and then expressed in true longitudes L (counted from Charon's orbital ascending node on J2000 mean equator) and radius r. This projection uses Charon's orbital pole of Tholen et al. (2008), see Table 5, and the star position given in Table 1. Our result is then

$$\begin{cases} X = +12, 070.5 \pm 4 \, \text{km} = +546.2 \pm 0.2 \, \text{mas}; \\ \quad L = 153.483 \pm 0°\!.071 \\ Y = +4, 576.3 \pm 25 \, \text{km} = +207.1 \pm 1.1 \, \text{mas}; \\ \quad r = 19,563.5 \pm 14 \, \text{km}, \end{cases}$$
(3)

for Charon's position with respect to Pluto, in the plane of the sky and in its orbital plane. This applies to 2008 June 22 at 69633.82 s UT (i.e., the Charon occultation mid-time at Les Makes), corresponding to JD 2454640.129964 at Pluto, once the light travel time of 4.22360 hr is accounted for.

Figure 8 shows our determination of Charon's Plutocentric position (X, Y) in the sky plane (Equation (3)), compared to another solution (T08) described later. Figure 9 is an enlargement of the central region of Figure 8. Figure 10 shows our Charon's position projected in the (L, r) plane, with Figure 11 being an expanded version of Figure 10. This result can now be used to discriminate between various Charon's orbital solutions. Before that, however, we examine possible biases in our measurements.

6. POSSIBLE SYSTEMATIC ERRORS

Two biases can alter our determination of Pluto and Charon's centers, specifically (1) asymmetries in Pluto's atmosphere and (2) timing errors at one or several stations. We examine those possibilities in turn.
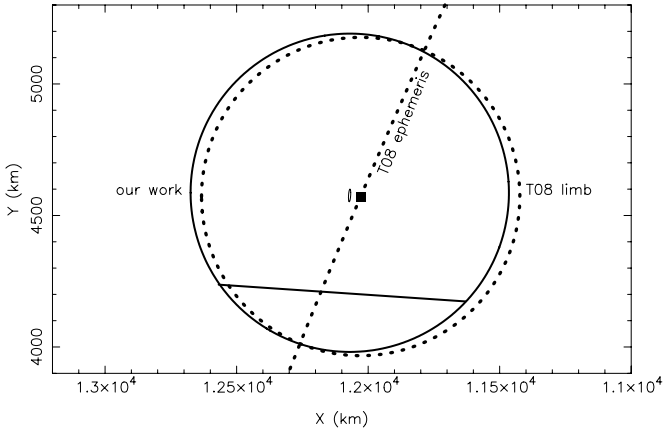
Figure 8. Fit of Charon's limb (assumed radius $R_C = 605$ km, solid circle, see the text) to the occultation chord (the almost horizontal straight line). The quantity X (resp. Y) is Charon's offset with respect to Pluto's center, counted positively toward the celestial J2000 east (resp. north) direction in the sky plane. The small central elongated ellipse is our estimated error ellipse for Charon's center, see also Figure 9. At that scale, Charon's position expected from the PLU017 ephemeris is almost undistinguishable from our fit shown here, see a better view in Figure 9. The dotted circle is Charon's limb as expected from the T08 ephemeris, while the dotted inclined line is Charon's Plutocentric motion expected from that same ephemeris. The black square is the expected T08 position of Charon's center at stellar closest approach.
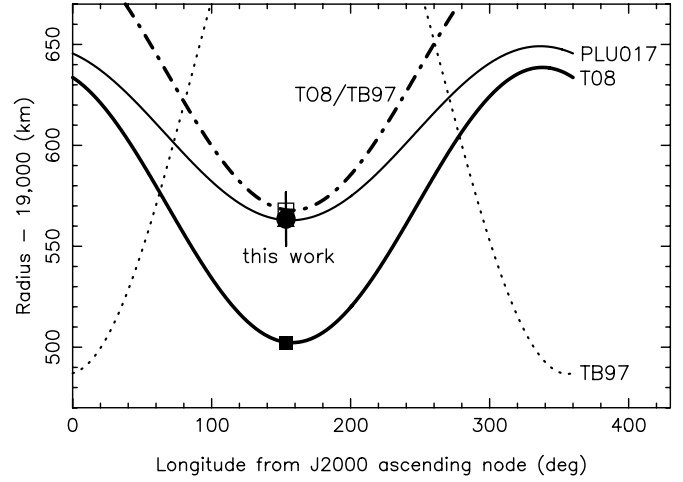

Figure 9. Enlargement of central part of Figure 8. The elongated ellipse is our estimated error ellipse for Charon's center derived in this paper (black dot) at stellar closest approach, 69633.82 s UT. The thick oblique solid line on the right shows Charon's motion with respect to Pluto expected from T08, with the black square marking the position at that 69633.82 s UT. Thin solid line: motion expected from PLU017, the black triangle marking the expected position, again at the same time. Dash-dotted line: expected Charon motion according to solution "T08/TB97," i.e., using the orbital elements of T08, except for the semi-major axis, which has been fixed to the TB97 value, $a = 19636$ km, see the text. The open square is the expected position from T08/TB97. The arrow shows the direction of Charon's motion relative to Pluto in the sky plane.

6.1. Effect of Possible Atmospheric Asymmetries

During light curve fitting, we have assumed that Pluto's atmosphere is spherically symmetric and centered on Pluto's center of mass. In reality, it may be distorted due to temperature and pressure contrasts, zonal winds, gravitational asymmetries, or other unknown effects.

Ellipticities of Pluto's atmosphere as high as ~6.6% and 9.1% have been reported by Person (2006), from the analyses of stellar occultations observed in 2002 and 1988, respectively.

Figure 10. Same as Figure 9, but projected in the (L, r) (radius, true longitude) plane. The same symbols and line styles as for Figure 9 are used. The error ellipse associated with our Charon's position (black dot) appears here as a small vertical tick mark. It is better resolved in Figure 11. For completeness, we have also drawn the T97 orbital solution (Tholen & Buie 1997) as a dotted line. Our measurement rules out solutions TB97 and T08, and is compatible with both solutions PLU017 and T08/TB97.
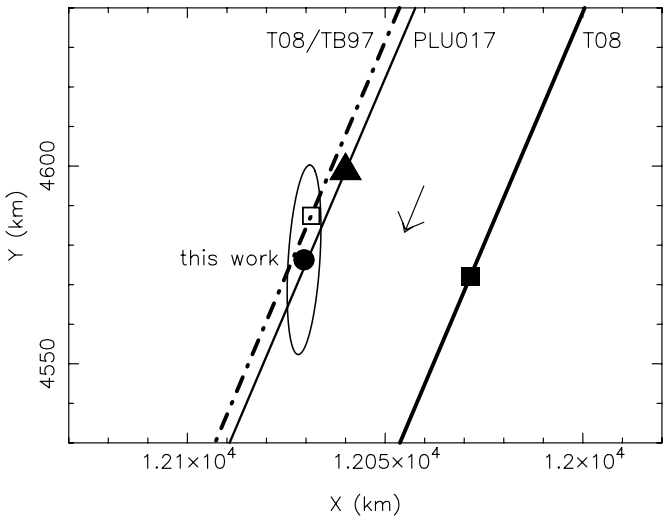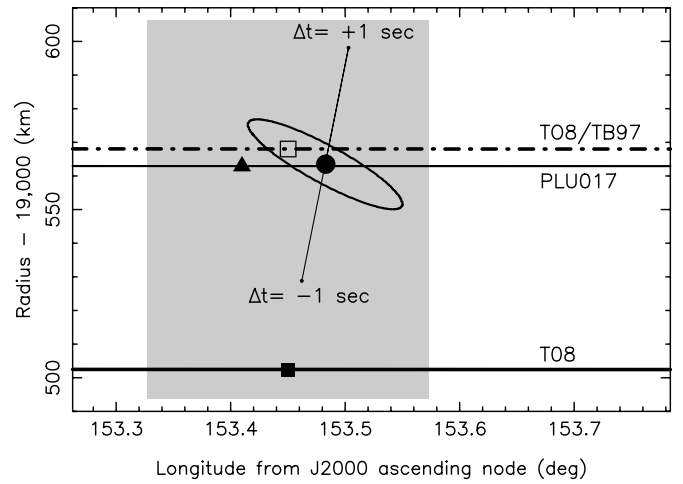

Figure 11. Enlargement of Figure 10, showing a closer view of our derived Charon's position (black dot) on JD 2454640.129964 at Pluto. The associated error ellipse is the projection of the error ellipse of Figure 9 in the (L, r) plane. Scales in longitude and radius have been adjusted so that the corresponding scales in km are the same along those two axes. The symbols are the same as in Figure 9. The gray area shows the uncertainty in longitude (but not in radius) on the T08 and T08/TB97 solutions (solid and open squares), stemming from the uncertainty on the T08 Charon's mean motion (Tholen et al. 2008). The thin, almost vertical, oblique line with extremity labeled "$\Delta t = -1$ s" (resp. "$\Delta t = +1$ s") shows Charon's position if -1 s (resp. $+1$ s) were added to the Charon occultation timing at Les Makes station. This segment illustrates the sensitivity of our results to potential time shifts at Les Makes.

In both cases, the semi-minor axis of the fitted ellipses are not aligned with Pluto's spin axis or with Charon's position vector projected in the plane of the sky. Thus, such ellipticities cannot stem from a zonal wind regime coaxial with Pluto rotation nor from tidal effects (yet to be explained) caused by Charon. Those ellipticities have not been confirmed so far. Actually, another Pluto occultation observed in 2007 indicates, according to Person et al. (2008), that horizontal wind speed at typical radii of 1400 km should be less than 3 m s^{-1}. This is clearly too small for supporting ellipticities as high as 6.6% or 9.1% through centrifugal acceleration of a zonal wind regime.

Alternate explanations are proposed to explain those putative distortions, like a nonsphericity of Pluto gravitational field, but those hypotheses still need to be confirmed. On our side, we do not have accurate enough photometric calibration to constrain the contribution of the planet to the occultation light curves, i.e., to constrain the zero stellar flux level Φ_0 defined before. As a consequence, we cannot include ellipticity as a free parameter in our fit, as it is strongly correlated with Φ_0.

Another issue stems from the fact that ingress sub-occultation points receive larger insolations than egress points during the event, a potential cause for atmospheric asymmetries. For instance, the Bankstown ingress sub-occultation point is near latitude $-39°$, while the egress point is near $+48°$ (Table 3). Since the sub-solar latitude is $-41°.2$, the ingress point receives almost permanent insolation, while egress corresponds to a region in almost permanent darkness. Thus, one might expect a significant difference in the ingress and egress temperature profiles, causing an atmospheric asymmetry in the isothermal branch of the profiles that would displace the retrieved Pluto center. However, none of the Pluto occultations observed so far shows evidences for a temperature contrast between summer and winter hemispheres, see, e.g., Sicardy et al. (2003), Elliot et al. (2007), and Young et al. (2008).

Young et al. (2008) comment on this paradoxical situation, analyzing a high signal-to-noise ratio (S/N) Pluto occultation light curve obtained in 2006. Although their sub-occultation point probed at egress receives sunlight for a diurnally averaged duration about seven times less than for ingress, the corresponding ingress and egress temperatures are not significantly different. These authors estimate that in this case, the expected egress temperature should be 92 K, significantly smaller than the observed 106.4 ± 4.6 K. Consequently, some dynamical processes, still to be described, must operate over sufficiently short timescales to counteract the expected cooling in region receiving small amounts of insolation. A possibility is the existence of horizontal winds between poles and equator. Estimating radiative time constants to some months or years, Young et al. (2008) conclude that horizontal winds of some meters per second are necessary in order to homogenize temperatures at all latitudes on timescales of days. Indeed, the possibility of horizontal winds of this magnitude, forced by solar-induced sublimation of nitrogen patches on Pluto's surface, is considered by Toigo et al. (2010).

We will not investigate further global circulation models in Pluto's atmosphere and we will assume, based on observational evidences, that no significant temperature differences are present in the upper atmosphere between the various sub-occultation points considered here. As commented before, all observations indicate that the upper isothermal branch of Pluto's atmosphere has a temperature T_∞ in the range 100–115 K, causing systematic biaises of ± 5 km at most on the retrieved geometry of the event.

This being said, Figure 11 shows that in order to discriminate between the various Charon's orbital solutions examined later, we have to pin down Charon's orbital radius, not its longitude. This means that we are mainly concerned with possible errors along the small axis of the error ellipse shown in that figure, which is close to the direction of motion of the star projected in Charon's orbital plane (illustrated by the small oblique line labeled $\Delta t = \pm 1$ s in Figure 11). Stated otherwise, constraints on Charon's radial Plutocentric position depend on how well Pluto's center position is determined along the direction of the occultation chords.

Note that in Figure 2 and Table 3 our occultation chords cover a large part of the morning Pluto's hemisphere, from southern latitudes ($\approx 38°$–$39°$ S at Bankstown and Blue Mountains, ingress) to high northern latitudes ($\approx 48°$N at Bankstown, Blue Mountains and Reedy Creek, egress), this latitude being almost the northernmost accessible to observation, $48°.8$, since the Plutocentric sub-observer latitude is $41°.2$S, see Table 1.

Consequently, most of the constraints on Pluto's center position along the direction of the chords come from the nearly central chords of Bankstown and Blue Mountains. In particular, we will see that in order to reconcile the so-called solution T08 (see Section 7.1) with our observation would require that Pluto's center is shifted by about 40 km, essentially toward east in the sky plane, with respect to the middles of those diametric chords, see Figure 9. This cannot be achieved if the isobar surfaces are flattened symmetrically with respect to Pluto's equatorial plane. In that case, the almost diametric chords of Bankstown and Blue Mountains would have their middles coinciding with the planet center. Thus, not only the atmosphere should be distorted, but this distortion should also be asymmetric between the ingress (southern) and the egress (northern) hemispheres.

So, let us consider situation where the isobars are distorted axisymmetrically with respect to Pluto's rotation axis, but asymmetrically between the two hemispheres. Such distortions are indeed observed in other contexts, e.g., in Titan's atmosphere. Titan stellar occultations observed in 1989 and 2003 provide evidence for a global distortion of the satellite atmosphere, see Hubbard et al. (1993) and Sicardy et al. (2006b), respectively. The central flash detected in 2003 shows for instance that the 0.25 mbar isobar (250 km altitude) has a northern, winter polar radius 50 km smaller than its equatorial counterpart, while the southern, summer hemisphere remains basically spherical. A global circular fit to the 0.25 mbar isobar would therefore provide an offset (along Titan's rotation axis projection in the sky plane) of about 50 km/2 = 25 km, with respect to Titan's center of mass. Such distortion can indeed be supported by the centrifugal acceleration associated with zonal winds. If $v(\phi)$ is the magnitude of this wind at latitude ϕ, then hydrostatic equilibrium requires that

$$v^2(\phi) = -g \cos(\phi) \cdot \frac{r(\phi) \cdot r'(\phi)}{r(\phi) \sin(\phi) - r'(\phi) \cos(\phi)}, \quad (4)$$

where $r(\phi)$ is the radius of the isobar at ϕ, $r' = dr/d\phi$, and g is the acceleration of gravity, see Equation (8) of Sicardy et al. (2006b).[31]

In the case of Titan, this distortion was interpreted as the evidence for a northern jet peaking at $v = 215$ m s^{-2} around $\phi = 55°$N, with velocities tapering off to zero in the southern hemisphere. This regime has been independently confirmed by the Cassini CIRS instrument, see Flasar et al. (2005).

So, let us consider Pluto's southern (summer) hemisphere essentially spherical, while the northern (winter) hemisphere is flattened, with the half-light isobar having a radius $\sim$80 km smaller than the equatorial radius at the highest latitudes probed here, that is about $48°$ N. This would cause a global displacement of 40 km for the middle of the diametric chords of Bankstown or Blue Mountains. This difference of 80 km between $\phi = 0°$ and $\phi = 48°$ N would imply typical maximum gradients r' of ≈ -100 km rad^{-1} in the northern hemisphere. Using

---

[31] Note the typo in Equation (8) of Sicardy et al. (2006b), where θ should be replaced by ϕ.

$g = 0.54$ m s^{-2} for the acceleration of gravity at half-light level ($r_{1/2} \approx 1275$ km), one derives $v \sim 200$ m s^{-1} from Equation (4).

This implies marginally supersonic flow, as the speed of sound is $c_s \approx 200$ m s^{-1} for a pure molecular nitrogen atmosphere at $T \sim 100$ K. This is not prohibitive, as no shock would be associated with this flow, but this would indicate that a vigorous mechanism is at work to maintain this wind regime. We also note that the half-light level is at $r_{1/2} \approx 1280$ km, i.e., at typical altitudes of 90–110 km, knowing that current observations place Pluto's radius somewhere between 1170 and 1190 km (Lellouch et al. 2009). Consequently, an altitude variation of 80 km between equator and latitude 48° N for the half-light isobar would imply a very severe change of atmospheric structure between the equatorial and polar regions of the dwarf planet. This is not expected as the nitrogen surface ice buffers the atmosphere, and imposes a nearly uniform atmospheric pressure (and roughly constant temperature) near the surface because of vapor pressure equilibrium. Note that for Titan, a 50 km variation of altitude between equator and the pole for the isobar causing the central flash is not a problem, as the studied level (0.25 mbar) is almost 10 scale heights above the surface (1.4 bar), which is then little affected by this distortion.

In conclusion, displacing the center of Pluto's atmosphere by 40 km with respect to its center of mass through a zonal wind regime or nonspherical internal mass distribution, remains possible, but those hypotheses presently lack any firm observational confirmations and physical grounds.

6.2. Timing Issues

Among the six positive detections, four (Bankstown, Blue Mountains, Glenlee, and Les Makes) come from video recordings at 25 frames s^{-1}, with GPS UT time inserted in the images by a "KIWI On Screen Display (OSD)" system developed by G. Hitchcox in New Zealand.[32] In order to increase S/N, though, the full rate of 25 frames s^{-1} was not conserved in the output data. Images at Glenlee, Les Makes, Bankstown, and Blue Mountains were, respectively, averages of 3, 8, 32, and 32 frames, yielding exposure times of, respectively, 0.12 s, 0.32 s, 1.28 s, and 1.28 s. In those cases, care was taken to consider the mid-times of exposures when assigning a UT time to a given data point.

At the other two stations (Reedy Creek and Craigie), CCD images were taken. The Reedy Creek experiment used the WWVH shortwave radio signal broadcast from Hawaii to time the shutter opening and closing, while the Craigie timing was taken from an internet Network Time Protocol (NTP) server. In those two cases, and contrary to the video recordings, readout time is significant, so that a dead time exists between two frames, during which no photon is received from the sky (see Table 2). Again, mid-times of exposures were considered for associating a UT time to each data point.

Concerning the KIWI OSD systems, sufficient time was allowed at all stations, so that the GPS receivers could synchronize correctly with the satellites. At this point, a message is issued indicating that synchronization is achieved, and this was the case at the sites involved. If a problem had been detected by the KIWI systems, the time displayed on the video frame would have flashed at a rate of 1 Hz, which was not observed.

When performing the simultaneous Pluto atmospheric fit to the five Australian light curves, we checked whether small

individual shifts in time at each station improved the fit. This allows us to detect potential timing problem at those stations, assuming that Pluto's atmosphere is spherical. In other words, we assume that the improvement of the fit in those cases are due to a correction of the timing, and not to a distortion of Pluto's atmosphere.

The sensitivity of the overall fit to individual timings is given in Table 3, where the 1σ error bars on the times of closest approach are obtained by increasing by $+1$ the minimum value of χ^2, or $\chi^2_{\min}$, obtained for the best fit. When doing so, we find that the Bankstown and Blue Mountains timings are mutually consistent to better than 0.1 s, well within the formal error bars of ± 0.25 s for both stations. This gives some credence that a correct absolute timing was obtained at those two stations using the KIWI OSD systems. Taking those times as benchmarks, we find that the Glenlee and Reedy Creek timings are lagging by -1.7 ± 0.6 s and -1.0 ± 0.5 s, respectively, while the Craigie timing is leading by 0.5 ± 3.3 s. Considering the error bars are at the 1σ level, those differences are not significant, even for the Glenlee station.

In any case, careful checks and analysis of previous occurrences of errors at Glenlee do not provide any evidence that a timing problem may have occurred there. The only possibility that might be retained is that the video recorder was switched off and on again while the KIWI system continued running. In that case, there are examples of a wrong time being inserted on the frames. However, this was not noted by the Glenlee observer, so that the -1.7 ± 0.6 s lag may be attributed to noise rather than timing, see Figure 6.

Concerning the Reedy Creek station, the -1.0 ± 0.5 s time lag is marginally significant. Mid-exposure times at the station are based on an audio of shutter events and a ticking quartz clock. The clock was then compared with the radio WWVH signal after the event, which showed that a $+0.07$ s time correction should be applied, besides a 0.04 s correction due to propagation time from the emitting station at Hawaii. The absolute time accuracy is estimated to be 0.02 s, although undetected errors caused by the operating system cannot be excluded.

Finally, we measure a formal, non-significant advance of $+0.5 \pm 3.3$ s (1σ) of the northernmost Australian chord (Craigie) with respect to Bankstown and Blue Mountains. The computer time used to stamp the CCD images is synchronized via an internet connection using an NTP server and is estimated to have an absolute accuracy of better than 0.5 s. Furthermore, visual checks, before and after the event, against a radio clock indicated that the computer did synchronize itself with the NTP server, as a non-synchronization would rapidly lead to a significant discrepancy between the computer and the radio clocks. Note that the relatively large error of ± 3.3 s error bar stems from the very grazing geometry of the event at Craigie (Figure 2), which poorly constrains the mid-time of the event (i.e., along Pluto's motion in the sky plane).

In conclusion, and considering the higher sensitivity of the fit to the nearly central chords obtained at Bankstown and Blue Mountains, it clearly appears that these two stations largely dominate the final value obtained for Pluto's offset along the planet motion in the plane of the sky, which is close to the east–west direction, see Figure 2. Stated otherwise, the value of the error bar on Δf_P given in Equation (1) relies essentially on the hypothesis that the Bankstown and Blue Mountains timings are correct, which is supported by the fact that their timings agree by better than 0.1 s.

---

[32] See descriptions in http://sites.google.com/site/kiwiosd/ and http://www.dangl.at/menu_gge.htm.

Table 5
Comparison of Our Results with Other Charon Orbital Solutions

			Charon Plutocentric orbital elements			
Source	a (km)	$e \times 10^3$	i^a (deg)	Ω^a (deg)	ω^a (deg)	P (days)
TB97[b]	$19{,}636 \pm 8$	7.6	96.163	222.993	356.1	6.387223
PLU017[c]	19,606.	2.2	96.1767	223.0514	156.4592	6.3872
T08[d]	$19{,}570.45 \pm 0.44$	3.484 ± 0.036	96.1680 ± 0.0028	223.0539 ± 0.0032	157.92 ± 0.32	6.387206 ± 0.000007
T08/TB97	19,636	3.484	96.1680	223.0539	157.92	6.387206

		Sky-plane Charon Plutocentric position on 2008 June 22, 69633.82 s UT[e]			
	X^f (km)	Y^f (km)	L^g (deg)	r^g (km)	
This paper	12070.5 ± 4	4576.3 ± 24	153.483 ± 0.071	$19{,}563.5 \pm 14$	
PLU017	12060.0	4598.8	153.410	19,562.9	
T08	12028.4	4572.1	153.450	19,502.2	
T08/TB97	12068.7	4587.4	153.450	19,568.0	

Notes. In this table, ω is the argument of periapsis, i.e., counted from ascending node to periapsis. Table 3 of Tholen & Buie (1997) gives instead the longitude of periapsis $\varpi = \Omega + \omega$.
[a] Mean equator and equinox of J2000.
[b] From Tholen & Buie (1997), Table 3.
[c] R. A. Jacobson (2009, private communication).
[d] From Table 4 of Tholen et al. (2008).
[e] Corresponding to JD 2454640.129964 at Pluto, once light travel time is accounted for.
[f] (X, Y) is the sky-plane Charon differential position with respect to Pluto, counted positively toward local east (right ascension) and toward north (declination) J2000 celestial directions, respectively.
[g] L is Charon's true longitude from J2000 ascending node; r is Charon's distance to Pluto's center. Our error bars on L and r are discussed in the text.

Concerning the Charon event, a potential problem is that it has been observed from only one station. Thus, no confirmation of its timing is provided by another independent experiment. As mentioned earlier, the timing at Les Makes was inserted into individual frames through a KIWI OSD system. Sufficient time was allowed at Les Makes to ensure correct synchronization of the GPS and the KIWI device, at which point a "FIX" message is issued to indicate that correct synchronization is achieved. Furthermore, in case a problem is detected by the system, the time displayed on the video frame flashes at a rate of 1 Hz, which was not the case for the Charon observation.

Timing problems were actually encountered at Les Makes during other observations. This happened when the video recorder was switched off while the KIWI system was still running. When switching on again the recorder, the displayed timing may be incorrect. However, care was taken during the Charon event that at no point the video recorder was switched off and on again.

We finally checked that the number of frames delivered by the video recorder at Les Makes corresponds to the time tags inserted on each frame, meaning that no time glitches occurred. Those tests were performed for all the sequences of observations made before (duration 35 s), during (duration 13 minutes), and after (respective durations 2, 2.3, and 2.1 minutes) the Charon event. On all five sequences, the numbers of frame match the time tags. Furthermore, we derive a rate of 49.9995 inter-frames s^{-1} from those countings, indicating a very small difference with the nominal announced value of 50 inter-frames s^{-1}, possibly caused by temperature influence on the quartz clock controlling the acquisition rate.

In conclusion, all the steps followed during the observation at Les Makes and all the checks performed a posteriori on the video tape indicate that the absolute timing at that station was correct to within a small fraction of a second.

It is instructive, however, to quantify the effect of a putative timing error at Les Makes on Charon's orbital position. Figure 11 shows the effect of a ± 1 s shift introduced in Les Makes timing. It shows that Charon's position is correspondingly changed by about $\pm 0.°020$ in longitude (or ± 7 km along the direction of orbital motion) and by ± 35 km in orbital radius. For instance, one should subtract 1.8 s to Les Makes timing to reduce Charon's orbital radius from 19,563.5 km (our result, Equation (3)) to the value $r = 19{,}502$ km predicted by the T08 solution (see discussion in Section 7.1).

In summary, we will assume in the rest of the paper that no timing error is affecting any of the stations in Australia and at Les Makes. We will also assume that Pluto's atmosphere is spherical, i.e., free of any distortion.

7. DISCUSSION

7.1. Comparison with Existing Orbital Solutions

We now compare our Charon position with those derived from four orbital solutions, referred here to as "TB97," "PLU017," "T08," and "T08/TB97" (see Table 5). This table also lists the orbital elements corresponding to each of these solutions.

Solution PLU017, used so far as a reference, is based on a fit to all Charon observations since discovery, except for the mutual event light curves. It includes image scale factors as estimated parameters during the fit, and also estimate Pluto's and Charon's masses (R. A. Jacobson 2009, private communication).

Solution T08 is mainly based on 384 images taken with the High Resolution Camera (HRC) mode of the Advanced Camera for Surveys (ACS) on the *HST* made in 2002–2003, even though 60 *HST* images taken in 1992–1993 are also used in the analysis, see Buie et al. (2006) and Tholen et al. (2008) for details.

Finally, solution T08/TB97 is a re-scaled version of solution T08, based on a former solution, TB97. The latter uses 60 *HST* observations made in 1992–1993, see Tholen & Buie (1997). More specifically, solution T08/TB97 uses all the orbital elements of T08, except for Charon's semi-major axis

($a = 19,570.45$ km), which is replaced by its TB97 value, $a = 19,636$ km. As discussed below in more details, although the TB97 solution is not well suited to describe Charon's orbital eccentricity, it is possibly better than T08 in terms of the general scaling of Pluto's system dimension, hence motivating the introduction of the T08/TB97 solution.

Table 5 provides the orbital elements associated with PLU017, T08, and T08/TB97, as well as the corresponding expected sky-plane Charon positions, together with our own measurement. Figure 10 shows that the PLU017 and T08 solutions agree well as far the longitudes of periapsis are concerned (they differ by less than $1°5$, see Table 5). They differ by more than 35 km in semi-major axis, and by a factor of about 1.6 in terms of orbital eccentricity. Conversely, solution TB97 strongly disagrees with both PLU017 and T08 solutions in terms of orbit orientation, with arguments of periapsis differing by more than $160°$ (Table 5).

Figure 9 shows that our measurement is compatible with the PLU017 position, with a barely significant shift of about $+25$ km along the direction of Charon's orbital motion in the plane of the sky, and a non-significant discrepancy of a fraction of km in the direction perpendicular to orbital motion. Our measurement indicates an insignificant $\approx +15$ km shift along Charon's orbital motion when compared to the T08 point but exhibits a clear discrepancy of about 40 km perpendicular to Charon's orbital motion.

When projected into the (L, r) plane, we can see in Figure 10 that our measurement clearly rules out solution TB97. Conversely, our position is consistent with the PLU017 solution, as it presents an offset of $+0.073 \pm 0°071$ (25 km) in longitude, and an offset of $+0.6 \pm 14$ km in radius, with respect to that solution, see Figure 11. Our measurement also agrees with the T08 solution in longitude, with an offset of $+0.033 \pm 0°071$ (11 km), but disagrees in the radial direction by $+61.3 \pm 14$ km.

We may assess the expected error in Charon's longitude by propagating the error on Charon's orbital period $P = 6.387206 \pm 0.000007$ days (Tholen et al. 2008) during the 2000 days or so between the epoch of the T08 solution (2002 November 22) and our observation. This results in a $\pm 0°12$ (corresponding to ± 40 km) error on the longitude of the T08 point, shown as the shaded gray zone in Figure 11. Note that the radial extent of that zone (i.e., along the vertical axis) has no particular meaning and does not represent the radial error bar on the T08 solution. Tholen et al. (2008) actually derive a typical radial uncertainty of a fraction of km for Charon's position, a small number that might need revision, see below.

So, the discrepancies in longitude between all the points plotted in Figure 11 remain well below the errors on the T08 orbital solution. In contrast, our $+61.3 \pm 14$ km radial discrepancy with the T08 solution is about 4.4 times larger than our expected error—much larger than the formal error of a fraction of km derived in Tholen et al. (2008).

Once the re-scaling of the T08 solution from $a = 19,570.45$ km to $a = 19,636$ km is applied, the agreement between our measurement and T08/TB97 is again (and by definition) $+0.033 \pm 0°071$ in longitude, but reduces to -4.5 ± 14 km in orbital radius. Although the agreement of our result with T08/TB97 appears formally better than for PLU017, discriminating between the two remains marginally possible using our measurement.

One may finally see in Figure 10 that the occultation occurred coincidentally near Charon's periapsis (as given by the PLU017 and T08 solutions), but also, and unfortunately, at the point where the PLU017 and T08/TB97 orbits are the closest, about 5 km in radial direction. Considering the sensitivity of our radial measurement (± 14 km), we would need to be at more than $60°$ from periapsis in order to discriminate between the PLU017 and T08/TB97 solutions.

7.2. Constraints on Orbital Solution

Two points are worth being discussed when comparing the four solutions PLU017, T08, TB97, and T08/TB97 with our measurement. They are (1) the possibility of pixel scale errors used to derive some of those solutions and (2) the possibility of center-of-light displacements caused by albedo features on Pluto and/or Charon. As both Pluto and Charon are synchronously locked, this may mimic an orbital eccentricity for Charon.

Image scale problems. The TB97 and T08 solutions differ by more 7σ in semi-major axes, pointing toward a possible scaling problem in at least one of the *HST* data sets (Tholen et al. 2008). Image scales were obtained with different methods in 1992–1993 (TB97) and 2002–2003 (T08) solutions, and a priori, there is no reason to prefer one method over the other (Ibid.). With that said, our measurement appears to rule out the semi-major axis derived from T08, while being in agreement with solution T08 rescaled to the semi-major axis of solution TB97.

Effect of albedo features. Conversely, and as discussed by Buie et al. (2006) and Tholen et al. (2008), the problem of center-of-light and center-of-mass displacement for Pluto was more precisely addressed in the 2002–2003 *HST* images, than in the 1992–1993 images, due to a more accurate modeling of the planet albedo map. In fact, the better spatial resolution of ACS HRC images recently allowed Buie et al. (2010b) to extract a more reliable Pluto's albedo map, hence permitting to extract the location of the center of mass.[33] Consequently, solution T08 should be preferred over solution TB97 as far as eccentricity and periapsis direction are concerned.

Note in passing in Figure 10 that the orbital eccentricity of solution TB97 is almost 2.2 times larger than for T08, with a direction of periapsis more than $160°$ away from T08. No plausible physical effect (e.g., perturbations by Nix and Hydra) can explain such discrepancy between 1992–1993 and 2002–2003 (Tholen et al. 2008), and indeed our measurement rules out solution TB97.

Note also that Charon's effect on a possible center-of-light displacement is negligible compared to Pluto's effect, with typical values of 20–40 km ($\sim$1–2 mas), see Buie et al. (2010b). Charon has about half the diameter of Pluto, and its photometric light curve has an amplitude in magnitude of $\Delta m \sim 0.08$, versus $\Delta m \sim 0.26$ for Pluto (Buie et al. 2010a), indicating a much more homogeneous albedo map.

No details on center-of-light corrections are presently available concerning solution PLU017. However, as the latter is based on 2002–2003 *HST* data, but also older images for which no albedo map modeling was applied, the T08 solution should be preferred over PLU017, in our opinion, as far as semi-major axis and eccentricity are concerned.

A possibility exists that the pixel scale of the 2002–2003 *HST* images is in fact correct, but that Charon's orbital eccentricity is negligible, corresponding to a circular orbital radius close to the T08 semi-major axis, $a = 19,570.45$ km. Our measured Charon's Plutocentric distance is indeed consistent with that

---

[33] The latter may be displaced by more than 100 km ($\sim$5 mas) with respect to the center of light.

value, $r = 19,563.5 \pm 14$ km. In that case, the eccentricities appearing in solutions PLU017 and T08 would be artifacts entirely caused by an erroneous modeling of Pluto center-of-light displacements. Such displacements, however, should not only mimic a radial excursion, but also, a longitudinal one. For instance, T08 orbital eccentricity, $e = 0.003484$, implies a total radial excursion of $2ea \approx 136$ km, or about 6 mas, and a total longitudinal excursion of $4ea \approx 272$ km, or about 12 mas, while the rms residual for the 384 Charon images, using solution T08, is about 2 mas (Tholen et al. 2008). So, mimicking an eccentric Charon orbit through albedo features on Pluto would require the right behavior in both radial and longitudinal directions. Although this is possible, an orbital eccentricity for Charon presently appears as the most likely interpretation of the 2002–2003 *HST* observations.

8. CONCLUSIONS

We have observed a stellar occultation on 2008 June 22 that involved both Pluto and Charon. From that event, we have derived Charon's Plutocentric position at a given instant (see Equation (3) and Figure 11). This position can be compared with existing orbital solutions, namely, solution T08 (Tholen et al. 2008), solution TB97 (Tholen & Buie 1997), solution T08 rescaled to the semi-major axis of solution TB97 (called here T08/TB97), and solution PLU017 (R. A. Jacobson 2009, private communication).

It must be emphasized that all the conclusions presented here assume that (1) the timings at the most central stations for the Pluto event (Bankstown and Blue Mountains) and at Les Makes station (Charon event) are correct and (2) Pluto's atmosphere is not distorted at a few tens of kilometers level. As discussed earlier, precautions were taken to obtain a correct timing on each image during the occultations, and specific tests performed after the observations did not reveal any timing problem at Les Makes station. As to atmospheric distortions in Pluto, although they cannot be ruled out, they are not presently supported by other observations. In any case, displacing our Pluto's center position by 40 km, so that to reconcile our measurement with the T08 orbital solution, would require marginally supersonic winds and a drastic modification of pressure profiles from equatorial to polar regions. In any case, those considerations show the paramount importance of good absolute timings in occultation events.

This being said, the following conclusions can be drawn from our results, as summarized in Equation (3), Figure 11, and Table 5. (1) Our measurement agrees well in longitude with both PLU017 and T08 solutions, with discrepancies of only 0.073 ± 0.071 and 0.033 ± 0.071 with those solutions, respectively. This is well inside the error bar on Charon's longitude, ± 0.12, obtained by propagating the error bar on mean motion provided of Tholen et al. (2008) from 2002 to 2008. (2) We find that Charon's radial distance to Pluto, in the satellite orbital plane, agrees at a fraction of km level with solution PLU017, well within our error estimation of ± 14 km. (3) Our Charon Plutocentric distance is about 61 km larger than that predicted by solution T08, that is 4.4 times our estimated error of ± 14 km. This rules out solution T08 and points toward a scaling problem for that solution. (4) Rescaling solution T08 (semi-major axis $a = 19,570.45$ km) to the semi-axis of solution TB97 ($a = 19,636$ km), while keeping all other orbital elements of T08 equal, reconciles our Charon radial distance with the new solution T08/TB97 to within 4.5 km, again well inside our estimated error.

In summary, our result may help solving the origin of the discrepancy between the TB97 and T08 solutions. The 7σ difference in semi-major axis between the two solutions would be caused by a slight error in the image scale determination of the HRC ACS of *HST*, while the better resolution of that instrument, and the resulting better Pluto's albedo map, would favor the T08 solution as far as Charon's orbital eccentricity and periapsis orientation are concerned.

Our result cannot discriminate between solutions T08/TB97 and PLU017, which are too close to each other at the particular longitude probed by the occultation. However, independent of our observation, we estimate that solution T08/TB97 should be preferred over solution PLU017. This is because the former takes into account a recent Pluto albedo map and is mainly based on the better 2002–2003 *HST* images, while the latter also includes older data for which center-of-light corrections were not made.

If adopted, solution T08/TB97 would mean that the 2002–2003 *HST* images have a pixel scale which is too small by a fractional amount of $(19,636–19,570.45)/19,570.45 = 3.35 \times 10^{-3}$. As all T08 orbital elements except semi-major axis a are retained in T08/TB97, this would also imply that the masses derived in Tholen et al. (2008) should be revised. From Kepler's third law, a relative increase $\delta a/a$ of semi-major axis results in a relative increase of $\delta M/M = 3\delta a/a \approx 1\%$ on all masses, and thus also densities.

Another consequence of this rescaling is that Nix and Hydra's orbits should also be expanded by 3.35×10^{-3}, compared to their values tabulated in Tholen et al. (2008). This implies increases of 165 km and 220 km for Nix and Hydra's semi-major axes, respectively, and represents two to three times their respective roughly estimated diameters of 88 and 72 km (Tholen et al. 2008). This is also comparable to the uncertainties on sky-plane positions for those satellites ∼200–350 km, as estimated by the same authors when propagating errors from 2002–2003 to the forthcoming period 2010–2015.

Clearly, more observations of stellar occultations involving both Pluto and Charon are welcome. As Pluto's system is now moving in front of the galactic center, the number of occultations has been increasing drastically in the last few years. So, although a double occultation remains rare, the probability of such an occurrence is not overwhelmingly small. In another paper (Assafin et al. 2010), predictions of occultations by Pluto, Charon, Nix, and Hydra are presented for the period 2010–2015, some of them potentially involving Pluto and one of its satellites.[34]

In terms of occultation predictions, Charon's current Plutocentric ephemeris is accurate enough (2–3 mas level, versus a Charon's angular diameter of 55 mas), so that corrections based on the present paper are irrelevant, since prediction accuracies of 15–20 mas at best can currently be reached. Concerning occultations by Nix and Hydra, the scaling corrections to T08 brought by this paper implies radial sky-plane shifts of up to 7–10 mas (compared to Nix and Hydra's angular diameters of 4–5 mas). This is still small compared to predictions accuracies, but not so small as for Charon, and might deserve consideration for occultation predictions.

---

[34] See http://www.lesia.obspm.fr/perso/bruno-sicardy/ to obtain the circumstances of those events.

APPENDIX

GENERATING SYNTHETIC LIGHT CURVES

The synthetic light curves are obtained through a ray-tracing code. We assume a pure and transparent nitrogen (N_2) atmosphere, with spherical symmetry centered on Pluto's center of mass. The stellar ray bending is calculated by dividing the atmosphere in 100 m thick layers, see details on the method in Sicardy et al. (1999). More precisely, starting from a prescribed temperature profile $T(r)$, fixing a boundary condition for pressure p, assuming hydrostatic equilibrium, and ideal gas law $p = nkT$ (where k is the Boltzmann' constant), we derive the nitrogen density profile n as a function of distance r to Pluto's center integrating:

$$\frac{1}{n} \cdot \frac{dn}{dr} = -\left[\frac{\mu g(r)}{kT} + \frac{1}{T}\frac{dT}{dr} \right], \qquad (A1)$$

from which a refractivity profile $\nu(r) = K_{N_2} \cdot n(r)$ is derived, using published refractive properties of N_2, see Table 1. This table also lists Pluto's physical parameters, from which the planet orientation and acceleration of gravity $g(r) = GM/r^2$ can be derived.

The pressure boundary condition is a value p at some prescribed radius r, e.g., the pressure p_0 at the deepest point considered, r_0. This provides the initial condition for n in Equation (A1), once $T(r)$ is specified. Thus, changing p_0—using the same profile $T(r)$—will change the pressure at all levels in the same relative way.

The adopted temperature profile is shown in Figure 4 and is referred to herein as the "nominal profile." It starts with an inversion layer at a minimum radius $r_0 = 1187.5$ km from Pluto's center, with a pressure of 9.82 μbar and a temperature gradient of $(dT/dr)_i = +7$ K km^{-1} which prevails in most of the inversion layer. The inversion layer then connects itself to an isothermal branch at $T_\infty = 107$ K above ~1210 km, with a pressure of 5.06 μbar at $r = 1215$ km, see details in the caption of Figure 4. More precisely, the temperature profile is obtained from the branch of a hyperbola:

$$T(r) = T_\infty + \left(\frac{dT}{2dr} \right)_i \cdot \left[(r - r_k) - \sqrt{(r - r_k)^2 + l^2} \right], \quad (A2)$$

where $l = 3$ km is a smoothing parameter which avoids a discontinuity of dT/dr near the "knee" taken at $r_k = 1197.4$ km.

The choice of this particular model follows from the best global fit to the five occultation light curves considered here and from previous works by other teams, see the text. We also discuss in the text the error bars on the particular values of $(dT/dr)_i$, r_k, and T_∞ adopted here, and their effects on the retrieved Pluto center.

REFERENCES

Assafin, M., Camargo, J. I. B., Vieira Martins, R., Andrei, A. H., Sicardy, B., Young, L., da Silva Neto, D. N., & Braga-Ribas, F. 2010, A&A, 515, A32
Buie, M. W., Grundy, W. M., Young, E. F., Young, L. A., & Stern, S. A. 2006, AJ, 132, 290
Buie, M. W., Grundy, W. M., Young, E. F., Young, L. A., & Stern, S. A. 2010a, AJ, 139, 1117
Buie, M. W., Grundy, W. M., Young, E. F., Young, L. A., & Stern, S. A. 2010b, AJ, 139, 1128
Elliot, J. L., et al. 2003, Nature, 424, 165
Elliot, J. L., et al. 2007, AJ, 134, 1
Flasar, F. M., et al. 2005, Science, 308, 975
Giorgini, J. D., et al. 1996, BAAS, 28, 1158
Gulbis, A. A. S., et al. 2006, Nature, 439, 48
Hubbard, W. B., et al. 1993, A&A, 269, 541
Lellouch, E., Sicardy, B., de Bergh, C., Käufl, H.U., Kassi, S., & Campargue, A. 2009, A&A, 495, L17
McDonald, S. W., & Elliot, J. L. 2000, AJ, 120, 1599
Ochsenbein, F., Bauer, P., & Marcout, J. 2000, A&AS, 143, 23
Pasachoff, J. M., et al. 2005, AJ, 129, 1718
Person, M. J. 2006, PhD thesis, Massachusetts Institute of Technology
Person, M. J., Elliot, J. L., Gulbis, A. A. S., Pasachoff, J. M., Babcock, B. A., Souza, S. P., & Gangestad, J. 2006, AJ, 132, 1575
Person, M. J., et al. 2008, AJ, 136, 1510
Sicardy, B., et al. 1999, Icarus, 142, 357
Sicardy, B., et al. 2003, Nature, 424, 168
Sicardy, B., et al. 2006a, Nature, 439, 52
Sicardy, B., et al. 2006b, J. Geophys. Res. (Planets), 111, E11S91
Stansberry, J. A., Lunine, J. I., Hubbard, W. B., Yelle, R. V., & Hunten, D. M. 1994, Icarus, 111, 503
Strobel, D. F., Zhu, X., Summers, M. E., & Stevens, M. H. 1996, Icarus, 120, 266
Tholen, D. J., & Buie, M. W. 1997, Icarus, 125, 245 (TB97)
Tholen, D. J., Buie, M. W., Grundy, W. M., & Elliott, G. T. 2008, AJ, 135, 777 (T08)
Toigo, A. D., Gierasch, P. J., Sicardy, B., & Lellouch, E. 2010, Icarus, 208, 402
Washburn, E. W. 1930, International Critical Tables of Numerical Data: Physics, Chemistry and Technology, Vol. 7 (New York: McGraw-Hill), 11
Widemann, T., et al. 2009, Icarus, 199, 458
Yelle, R. V., & Lunine, J. I. 1989, Nature, 339, 288
Young, E. F., et al. 2008, AJ, 136, 1757